ACS NANO
Cite This: ACS Nano 2018, 12, 4594−4604
www.acsnano.org

ARTICLE

General Synthetic Strategy for Libraries of Supported Multicomponent Metal Nanoparticles

Hui Yang,[†,§,#] Siobhan J. Bradley,[‡] Xin Wu,[§] Andrew Chan,[∥] Geoffrey I. N. Waterhouse,[∥] Thomas Nann,[‡] Jian Zhang,[*,§] Paul E. Kruger,[*,⊥] Shengqian Ma,[*,#] and Shane G. Telfer[*,†]

[†]MacDiarmid Institute for Advanced Materials and Nanotechnology, Institute of Fundamental Sciences, Massey University, Palmerston North 4442, New Zealand

[‡]MacDiarmid Institute for Advanced Materials and Nanotechnology, School of Chemical and Physical Sciences, Victoria University of Wellington, Wellington 6140, New Zealand

[§]State Key Laboratory of Structural Chemistry, Fujian Institute of Research on the Structure of Matter, Chinese Academy of Sciences, Fuzhou 350002, P.R. China

[∥]MacDiarmid Institute for Advanced Materials and Nanotechnology, School of Chemical Sciences, The University of Auckland, Auckland 1142, New Zealand

[⊥]MacDiarmid Institute for Advanced Materials and Nanotechnology, School of Physical and Chemical Sciences, University of Canterbury, Christchurch 8140, New Zealand

[#]Department of Chemistry, University of South Florida, CHE205A, 4202 East Fowler Avenue, Tampa, Florida 33620, United States

Supporting Information

ABSTRACT: **Nanoparticles comprising three or more different metals are challenging to prepare. General methods that tackle this challenge are highly sought after as multicomponent metal nanoparticles display favorable properties in applications such as catalysis, biomedicine, and imaging. Herein, we report a practical and versatile approach for the synthesis of nanoparticles composed of up to four different metals. This method relies on the thermal decomposition of nanostructured composite materials assembled from platinum nanoparticles, a metal−organic framework (ZIF-8), and a tannic acid coordination polymer. The controlled integration of multiple metal cations (Ni, Co, Cu, Mn, Fe, and/or Tb) into the tannic acid shell of the precursor material dictates the composition of the final multicomponent metal nanoparticles. Upon thermolysis, the platinum nanoparticles seed the growth of the multicomponent metal nanoparticles *via* coalescence with the metallic constituents of the tannic acid coordination polymer. The nanoparticles are supported in the walls of hollow nitrogen-doped porous carbon capsules created by the decomposition of the organic components of the precursor. The capsules prevent sintering and detachment of the nanoparticles, and their porosity allows for efficient mass transport. To demonstrate the utility of producing a broad library of supported multicomponent metal nanoparticles, we tested their electrocatalytic performance toward the hydrogen evolution reaction and oxygen evolution reaction. We discovered functional relationships between the composition of the nanoparticles and their electrochemical activity and identified the PtNiCu and PtNiCuFe nanoparticles as particularly efficient catalysts. This highlights how to generate diverse libraries of multicomponent metal nanoparticles that can be synthesized and subsequently screened to identify high-performance materials for target applications.**

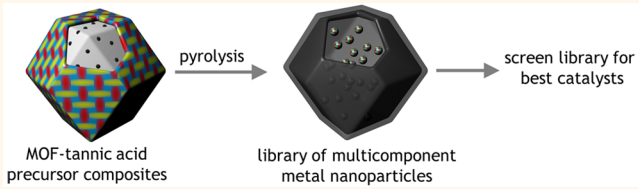

KEYWORDS: *metal−organic framework, multicomponent, metal nanoparticles, electrocatalysts, water splitting*

The integration of multiple different metals into nanoparticles presents formidable challenges as the constituents tend to separate into an ensemble of individual phases or to aggregate in an uncontrolled manner.[1−6] General synthetic methods to multicomponent metal nanoparticles (MMNPs) are highly sought after as they can exhibit properties that do not arise in their single-component counterparts. In particular, when the components of MMNPs blend into homogeneous alloys, attractive chemical, electronic, and magnetic properties frequently emerge. Due to these favorable characteristics, alloyed nanoparticles are deployed in a range of applications such as chemical catalysis,[7−9] electro-

Received: February 6, 2018
Accepted: April 10, 2018
Published: April 18, 2018

DOI: 10.1021/acsnano.8b01022
ACS Nano 2018, 12, 4594−4604

catalysis,[3,10−17] medicine,[18−20] and magnetic imaging.[21−23] Although a breadth of approaches to the synthesis of binary MMNPs exists, general synthetic routes to MMNPs that integrate three or more different elements are rare.[7,14,17] In a notable recent contribution, a polymer nanoreactor-mediated synthesis method was reported to produce a combinatorial library of multimetallic nanoparticles.[24] While this work is a beautiful realization of a diverse library of MMNPs unattainable by conventional methods, it is not readily conducive to the synthesis of MMNPs at scale. To bridge the exquisite properties of MMNPs with their growing body of applications, robust and scalable synthetic methods are a pressing challenge.

In this context, we hypothesized that a general route to libraries of supported MMNPs could be based on assembling the metal constituents in suitably designed precursor materials fabricated from readily available starting compounds. We recently discovered that monometallic or bimetallic nanoparticles supported on nitrogen-doped hollow porous carbon capsules (NPCCs) can be generated by the thermolysis of composites of metal−organic frameworks and tannic acid coordination polymers (Scheme 1).[25] Here, the metal−organic framework is ZIF-8. When coated with a coordination polymer comprising potassium tannic acid (K-TA), organic components of the composite form a hollow capsule upon pyrolysis. The tannic acid coordination polymer shell plays a crucial role in directing the formation of the hollow capsules; dense particles form in its absence. The integration of platinum nanoparticles (PtNPs) can be achieved by sandwiching them between the ZIF nanocrystal and the K-TA shell (Scheme 1, step I) to produce a composite material denoted as ZIF-8/Pt@K-TA. Pyrolysis of this material yields supported monometallic nanoparticles (Scheme 1, Route A). *Bimetallic* PtCo nanoparticles are produced if the potassium ions of the tannic acid layer are exchanged with cobalt(II) to give ZIF-8/Pt@Co-TA prior to pyrolysis (Scheme 1, Route B). Again, the tannic acid shell plays a vital role by bringing the seed PtNPs and the dispersed cobalt ions into close proximity. The cobalt ions are reduced to cobalt metal in the pyrolysis step. Owing to the ideal structure of the composite, no segregated unary PtNPs nor CoNPs are observed. Bimetallic PtCoNPs are generated as the exclusive product.

Scheme 1. Illustration of the Synthetic Routes to Various Types of Metal Nanoparticles Embedded in Nitrogen-Doped Porous Carbon Capsules

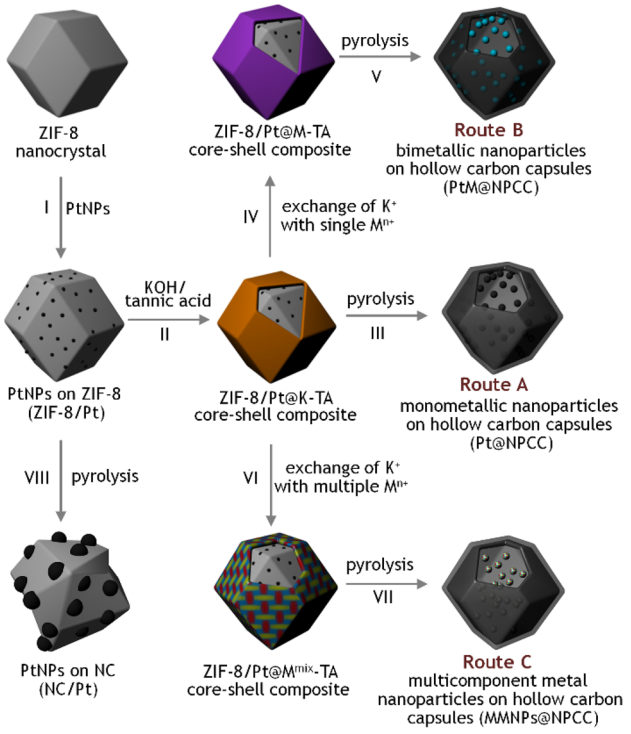

By capitalizing on these results, we sought to develop a practical method for the synthesis of libraries of MMNPs embedded in the walls of hollow porous nitrogen-doped carbon capsules (Scheme 1, Route C). We hypothesized that it should be possible to exchange the potassium ions in the K-TA shell by *multiple* metal ions to yield mixed-metal composites of the form ZIF-8/Pt@M^{mix}-TA, where M^{mix} is a mixture of two or more *different* metal ions. We illustrate this in step VI of Scheme 1. The subsequent pyrolysis of the ZIF-8/Pt@M^{mix}-TA composites (Route C, step VII, Scheme 1) is designed to produce supported MMNPs that comprise platinum along with two or three other components (MMNPs@NPCC). This step is designed to reduce the metal ions in the TA coordination polymer to their zero-valent state. Because intimate contact with the PtNP seeds is ensured by the ZIF-8/Pt@M^{mix}-TA composites, these metals should fuse to produce alloyed MMNPs. In principle, this protocol would be amenable to the formation of diverse libraries of MMNPs@NPCC materials given the variety of metal ions (M^{mix}) that can be incorporated into the tannic acid coordination polymer shell.

We report here the successful realization of this methodology and the generation of a diverse range of supported MMNPs. This straightforward fabrication method suppresses the uncontrolled nucleation of individual metal ion nanoparticles and prevents the formation of an ensemble of different phases. It is potentially scalable as it relies on readily available precursor compounds, and the manipulations are amenable to large quantities of materials. To demonstrate the utility of MMNP libraries, we outline their synthesis followed by a rapid screening assay to identify high-performance catalysts for electrolytic water splitting. We have focused on tri- and tetrametallic NPs to date; however, we anticipate that this proof-of-concept work could be extended to MMNPs containing an even larger number of components.

RESULTS AND DISCUSSION

As previously reported, ZIF-8/Pt@K-TA can be heated under hydrogen/argon (40/60) to produce Pt@NPCC, which features ∼5.5 nm platinum nanoparticles supported in the walls of hollow NPCC capsules (Scheme 1, Route A).[25] In this thermolysis process, the organic components of ZIF/Pt@K-TA are converted into hollow nitrogen-rich carbon capsules. These capsules are free of potassium and zinc: the potassium ions are eliminated by washing, and the zinc ions are reduced to zinc metal, which evaporates during pyrolysis. Whereas the PtNPs in ZIF-8/Pt@K-TA are initially too small to detect by powder X-ray diffraction (PXRD), upon thermolytic conversion to other materials, the PtNPs increase in size—by agglomeration and/or the inclusion of additional metals—and become detectable by PXRD (*vide infra*).

Extending this protocol to the synthesis of supported bimetallic nanoparticles, the pyrolysis of ZIF-8/Pt@Ni-TA results in hollow nitrogen-doped porous carbon capsules with platinum/nickel alloyed nanoparticles embedded in the capsule

DOI: 10.1021/acsnano.8b01022
ACS Nano 2018, 12, 4594−4604

walls (PtNi@NPCC). Scanning electron microscopy (SEM) images reveal the same capsule morphology observed for Pt@NPCC (Figure S13). TEM images confirm that the capsules are hollow and that the nanoparticles are deposited uniformly in the capsule walls (Figure 2a). The average diameter of the PtNiNPs in PtNi@NPCC is ~7.2 nm, which is consistent with the nickel atoms from the Ni-TA layer fusing with the Pt nanoparticles during pyrolysis to produce bimetallic PtNi nanoparticles (Figure S30). The PXRD pattern of PtNi@NPCC exhibits (111), (200), and (220) reflections at 2θ angles intermediate between those of Pt@NPCC (monometallic PtNPs) and Ni@NPCC (monometallic NiNPs), as illustrated in Figure 1. High-resolution transmission electron microscopy (HRTEM) images of individual PtNiNPs clearly reveal lattice fringes with an interplanar spacing of 2.14 Å, which equates to the contrast profiles of the (111) planes (Figure 2b). The peaks in the selected area electron diffraction (SAED) pattern of PtNi@NPCC can be indexed to the (111), (200), (220), and (311) planes of the alloyed PtNi nanoparticles (Figure 2j). These measurements indicate that the Pt and Ni atoms are alloyed in the nanoparticles, and this was confirmed by two additional measurements. First, STEM images and the corresponding elemental maps show that the Pt and Ni atoms are spatially colocated (Figure 2c–g). Second, an energy-dispersive spectroscopy (EDS) line scan analysis exhibited a uniform distribution of the Pt and Ni atoms (Figure 2h,i). X-ray photoelectron spectra (XPS) of PtNi@NPCC demonstrate the presence of platinum, nickel, carbon, and nitrogen (Figure S40). The Pt 4f and Ni 2p binding energies align closely with those previously reported for PtNi nanoparticles.[8,10] Inductively coupled plasma atomic emission spectroscopy (ICP-AES) analysis results show that the PtNiNPs supported on PtNi@NPCC contain 4 wt % Pt and 10.2 wt % Ni (Table 1). This equates to a Pt/Ni molar ratio of about 1:8, which correlates very closely with the Pt/Ni ratio found in the ZIF-8/Pt@Ni-TA precursor (Table S1). The high Ni content, previously observed in other PtNiNP materials, and the uniform mixing of the two metals are enabled by the similarity of their crystal structures (face-centered cubic (fcc) packing) and the melting of the PtNPs during pyrolysis.[25,26]

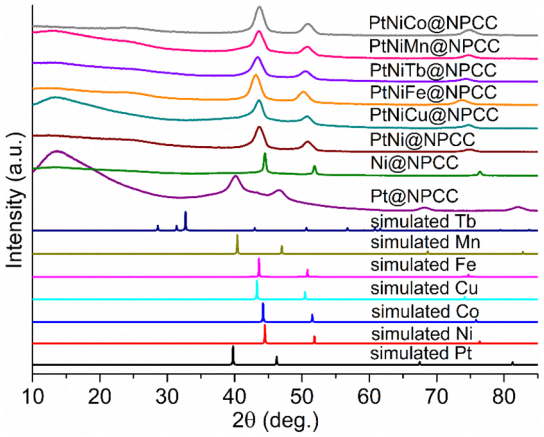

Figure 1. PXRD patterns of selected single- and multicomponent metal nanoparticles supported on hollow carbon capsules.

We then investigated the mechanism of formation of PtNi@NPCC. Pyrolysis of ZIF-8/Pt@Ni-TA was carried out in 100 °C steps between 500 and 900 °C, which was followed by immediate cooling. TEM and PXRD (Figures S4 and S17)

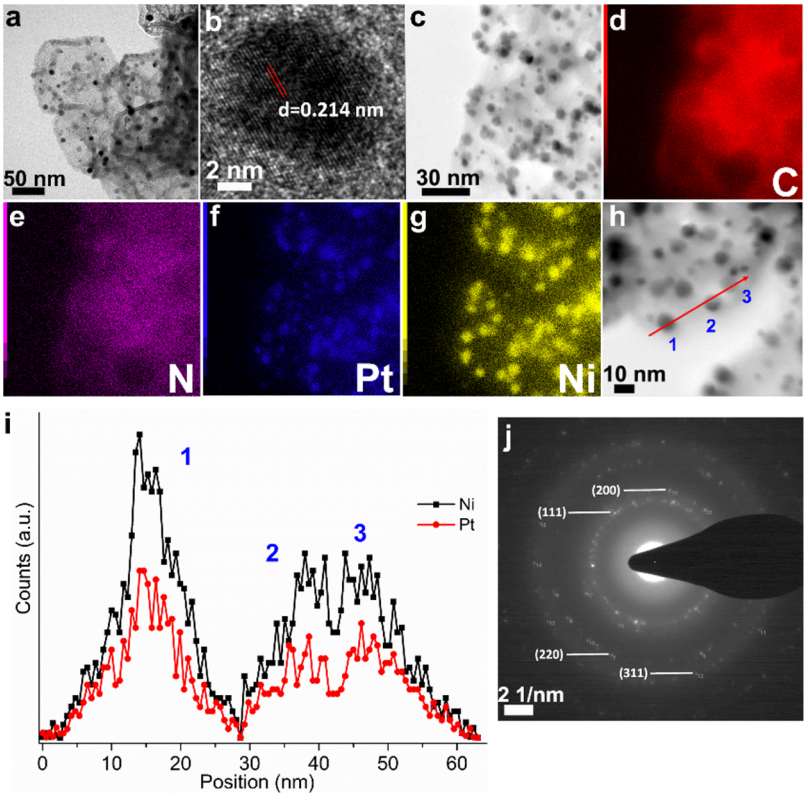

Figure 2. (a) TEM image of PtNi@NPCC. (b) HRTEM image of an individual PtNi nanoparticle. (c–g) STEM image and elemental mapping of PtNi@NPCC. (h,i) STEM image and EDS distributions of Pt and Ni along the arrow line on h. (j) SAED pattern of PtNi@NPCC.

DOI: 10.1021/acsnano.8b01022
ACS Nano 2018, 12, 4594–4604

Table 1. Summary of the Compositions and Textural Properties of the Porous Carbon Nanocapsules and Their Composites with Monometallic and Multicomponent Metal Nanoparticles[a]

material	precursor	Pt wt %	Ni wt %	M_1[b] wt %	M_2[b]	N wt %	BET[c]	pore volume[d]
NC	ZIF-8	n/a	n/a	n/a	n/a	n/d	1245[e]	0.67[e]
NPCC	ZIF-8@K-TA	n/a	n/a	n/a	n/a	n/d	685[e]	1.01[e]
Ni@NPCC	ZIF-8@Ni-TA	n/a	4.15	n/a	n/a	6.90	750[e]	0.93[e]
Pt@NPCC	ZIF-8/Pt@K-TA	6.22	n/a	n/a	n/a	1.82	842[e]	1.33[e]
PtNi@NPCC	ZIF-8/Pt@Ni-TA	4.00	10.2	n/a	n/a	1.48	588[e]	0.85[e]
PtNiFe@NPCC	ZIF-8/Pt@NiFe-TA	2.50	3.81	1.60	n/a	1.77	658	0.85
PtNiCo@NPCC	ZIF-8/Pt@NiCo-TA	3.25	6.38	1.11	n/a	1.90	717	0.88
PtNiTb@NPCC	ZIF-8/Pt@NiTb-TA	2.67	5.19	3.58	n/a	1.74	476	0.64
PtNiCu@NPCC	ZIF-8/Pt@NiCu-TA	2.31	4.21	1.12	n/a	1.80	681	0.94
PtNiMn@NPCC	ZIF-8/Pt@NiMn-TA	3.07	6.48	0.32	n/a	1.96	730	0.90
PtNiCuFe@NPCC	ZIF-8/Pt@NiCuFe-TA	1.88	3.08	0.71	0.49	1.92	680	0.64
PtNiCuTb@NPCC	ZIF-8/Pt@NiCuTb-TA	1.84	2.85	0.58	1.09	1.89	702	0.66

[a]n/a = not applicable; n/d = not determined. [b]M_1 = Fe, Co Tb, Cu, or Mn; M_2 = Fe or Tb; metal content determined by ICP-AES. [c]BET surface area in m^2/g determined by N_2 adsorption at 77 K. [d]Total pore volume in cm^3/g determined at 0.95 bar by N_2 adsorption at 77 K. [e]As reported in ref 25.

reveal the progressive evolution of PtNi@NPCC. A sandwich-like ZIF-8/Pt@carbon is initially formed by the pyrolysis of ZIF-8/Pt@Ni-TA at 500 °C, in which the Ni-TA layer has carbonized but the ZIF core is retained (Figures S4 and S17a). The carbon layer formed in this step serves as a template for the further deposition of the carbon shell. As the pyrolysis temperature increases to 600 and then to 700 °C, the ZIF-8 core decomposes to ZnO. Some of the ZnO is reduced to metallic Zn by hydrogen, and the genesis of capsule formation becomes evident at this point (Figures S4 and S17b). The density of the capsules is significantly reduced by 700 °C, indicating that the formation of the hollow capsule core is largely complete (Figure S17c). By heating to 800 and 900 °C, the ZnO is continually reduced to Zn metal, which then vaporizes and escapes from the material (Figures S4 and S17d,e). The alloyed PtNiNPs are formed at these higher temperatures. The PtNi (111) peaks observed by PXRD shift subtly with the pyrolysis, which indicates that the composition of the NPs varies with temperature (Figure S4). Upon pyrolysis at 900 °C for 3 h, PtNi@NPCC is produced, as in the direct synthesis method.

These results provide a platform for the synthesis of multicomponent metal nanoparticles comprising three or more different metals embedded in the walls of hollow carbon capsules. We set about this goal by exchanging *multiple* metal ions into the tannic acid coordination polymer shell prior to thermolysis (Route C in Scheme 1). Our initial experiments focused on replacement of the potassium ions in the K-TA shell by a mixture of nickel(II) and iron(III) ions to give ZIF-8/Pt@NiFe-TA. Inserting approximately equal quantities of these two metal ions was not straightforward due to their differing propensities for displacing potassium ions. However, by careful adjustment of the relative amounts of $Fe(NO_3)_3$ and $Ni(NO_3)_2$ added to the methanolic solution used for cation exchange, a ZIF-8/Pt@NiFe-TA composite with 2.23 wt % Ni/0.95 wt % Fe was produced (Table S1 and Figure S8e). TEM and SEM images of the resulting ZIF-8/Pt@NiFe-TA composite clearly reveal that the polyhedral morphology of the ZIF-8 nanocrystal template remains intact after the incorporation of iron(III) and nickel(II) into the TA layer (Figure S8a,b). PXRD showed that the crystallinity of the ZIF core is retained and that the NiFe-TA shell is amorphous, as expected (Figure S3).

The subsequent pyrolysis of ZIF-8/Pt@NiFe-TA resulted in the formation of hollow capsules that support alloyed trimetallic PtNiFe nanoparticles (Figure 3a). A breadth of experimental techniques supports this conclusion. SEM and TEM images demonstrate the existence of hollow capsules comprising nitrogen-doped carbon, with embedded metal nanoparticles (Figures 3a and S18a,c). The nanoparticles comprise three different metallic components (Pt, Ni, and Fe) with a random spatial distribution, as evidenced by high-resolution scanning transmission electron microscopy (Figures 3b and S18c). The average diameter of these PtNiFeNPs is ~7.3 nm (Figure S30), which is larger than that of the seed PtNPs and thus consistent with the incorporation of nickel and iron from the tannic acid shell into the PtNPs during pyrolysis. Each nanoparticle showed lattice fringes with an interplanar spacing of 2.17 Å, which corresponds to the contrast profiles of their (111) planes (Figure 3b). Their SAED pattern can be indexed to the (111), (200), (220), and (311) planes of alloyed PtNiFe nanoparticles (Figure 3g). STEM imaging, EDS mapping, and EDS line scans confirm that the three metal components are uniformly distributed (Figure 3c–f,h,i). The trimetallic nanoparticles exhibit diffraction peaks at 2θ = 43.3 and 50.1°, which can be assigned to the (111) and (200) reflections, respectively, of an fcc lattice (Figure 1). The shift to higher 2θ angles vis-à-vis pure PtNPs is consistent with the smaller size of Ni and Fe. XPS on PtNiFe@NPCC confirmed the presence of platinum, nickel, iron, carbon, and nitrogen (Figure S41). Pt $4f_{7/2}$ and Pt $4f_{5/2}$ bands were observed at 72.0 and 75.3 eV, which are in agreement with values reported for platinum metal in binary and ternary alloy systems.[8,10,27,28] The Ni $2p_{3/2}$ and Ni $2p_{1/2}$ peaks were observed at 853.1 and 870.4 eV, and Fe $2p_{3/2}$ and Fe $2p_{1/2}$ peaks were observed at 707.6 and 720.7 eV, together with a Ni Auger feature at 712.1 eV. These results are in accord with XPS data reported for zero-valent nickel and iron.[8,10,29,30] The Pt/Ni/Fe ratio in PtNiFe@NPCC (2.5 wt % Pt, 3.81 wt % Ni, and 1.6 wt % Fe) is 1:5.2:2.3, as determined by ICP-AES (Table 1). This is consistent with the ratio of Pt/Ni/Fe = 1:5.14:2.31 in the ZIF-8/Pt@NiFe-TA precursor (Table S1). The nitrogen content is 1.77 wt %, as determined by elemental analysis. XPS also allowed examination of the nitrogen speciation in the carbon supports (Figures S37–S47). We identified pyridinic N (398.5 eV), pyrollic N (400.0 eV), graphitic N (401.5 eV), and pyridinic oxide (405.5

DOI: 10.1021/acsnano.8b01022
ACS Nano 2018, 12, 4594–4604

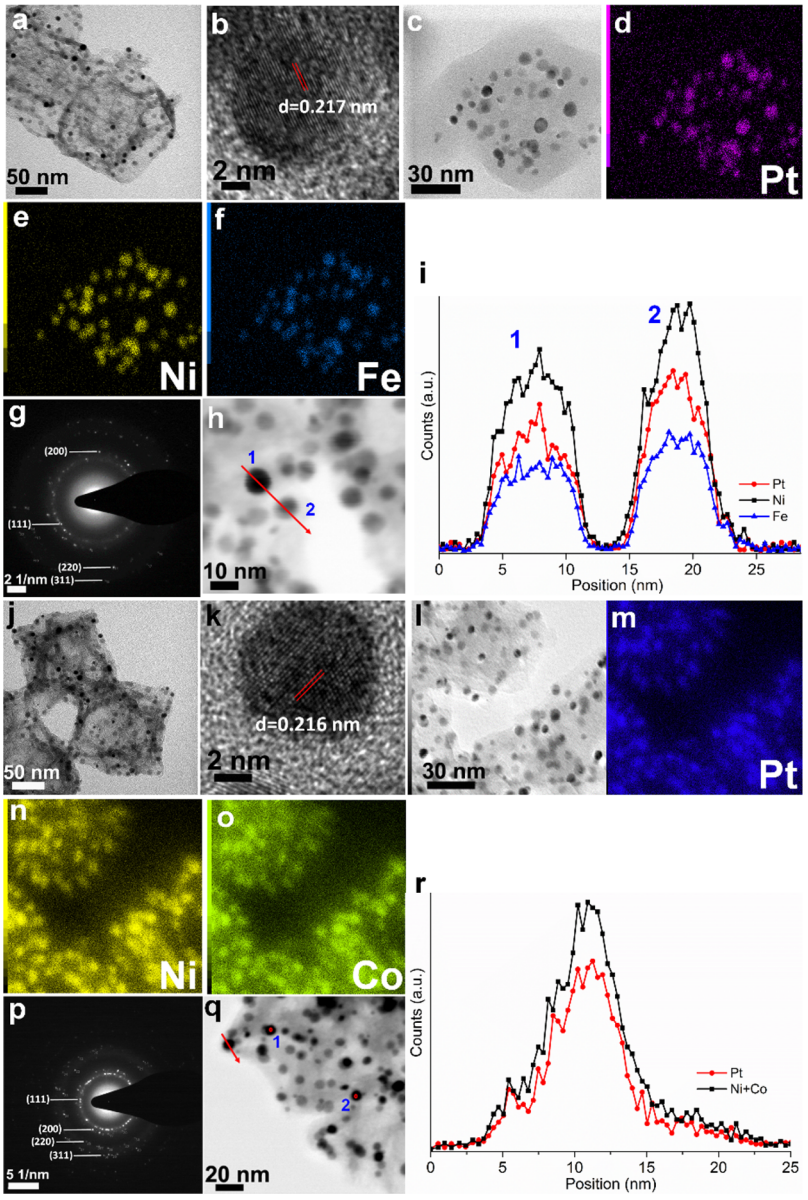

Figure 3. (a) TEM image of PtNiFe@NPCC. (b) HRTEM image of an individual PtNiFe nanoparticle. (c–f) STEM image and elemental mapping of PtNiFe@NPCC. (g) SAED pattern of PtNiFe@NPCC. (h,i) STEM image and EDS distributions of Pt, Ni, and Fe along the arrow line on h. (j) TEM image of PtNiCo@NPCC. (k) HRTEM image of an individual PtNiCo nanoparticle. (l–o) STEM image and elemental mapping of PtNiCo@NPCC. (p) SAED pattern of PtNiCo@NPCC. (q,r) STEM image and EDS distributions of Pt, Ni, and Co along the arrow line on q.

eV). N-doping reduces the hydrophobicity of carbon, whereas pyridinic N sites promote both oxygen evolution reaction (OER) and hydrogen evolution reaction (HER), which is of relevance to electrocatalytic water splitting tests discussed below. The Raman spectra for all samples show a prominent G-band; therefore, the carbon capsules are expected to possess good electrical conductivity, which will enhance their electrocatalytic performance (Figure S36).

We subsequently extended the fabrication method to other multicomponent metal nanoparticles. PtNiCo@NPCC, PtNiCu@NPCC, PtNiTb@NPCC, and PtNiMn@NPCC were synthesized by first introducing the different metal ions into the tannic acid shell of ZIF-8/Pt@M^{mix}-TA composites. Microscopy images and EDS spectra of the composite materials were consistent with their anticipated compositions (Table S1): ZIF-8/Pt@NiCo-TA (Figures S3 and S8c,d,f), ZIF-8/Pt@NiCu-TA (Figures S3 and S9a,b,e), ZIF-8/Pt@NiMn-TA (Figures S3 and S9c,d,f), and ZIF-8/Pt@NiTb-TA (Figures S3 and S10). A subsequent pyrolysis step at 900 °C reduced the metal ions and alloyed them with the PtNP seeds while simultaneously generating the hollow capsule support. The key properties of materials are summarized in Table 1. The metal and nitrogen contents of these composites were determined by ICP-AES and combustion elemental analysis, respectively. Characterization by PXRD, SEM, TEM, HRTEM, STEM, EDS elemental analysis, XPS (Figures S42–S45), and Raman spectroscopy (Figure S36) generated a similar structural picture to the PtNiFe@NPCC analogue: these materials comprise alloyed trimetallic nanoparticles embedded in the walls of hollow nitrogen-doped carbon capsules (Figure 3j–r and Figures S18–S21, S23–S26).

DOI: 10.1021/acsnano.8b01022
ACS Nano 2018, 12, 4594–4604

Nitrogen adsorption isotherms of the supported trimetallic nanoparticles were measured at 77 K. The isotherms showed a sharp uptake of N_2 at low relative pressure ($P/P_0 < 0.1$) and a gradual increase at higher relative pressure ($0.1 < P/P_0 < 0.95$), indicating the existence of both micro- and mesopores (Figure 4). The pronounced hysteresis loops observed toward higher

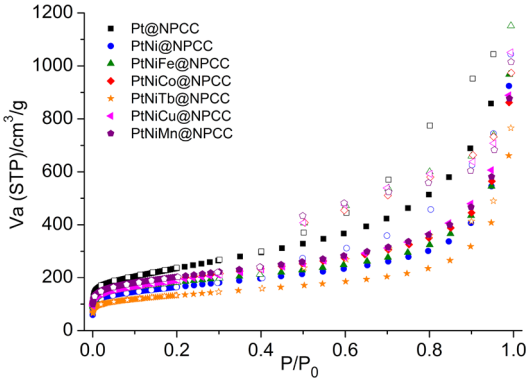

Figure 4. N_2 adsorption (filled symbols) and desorption (open symbols) isotherms of selected single- and multicomponent metal nanoparticles supported on hollow carbon capsules measured at 77 K.

pressures imply that the larger mesopores have semiclosed, ink-bottle shapes. The calculated Brunauer–Emmett–Teller (BET) surface areas of these materials fall in the range of 650–750 $m^2\ g^{-1}$ (Table 1). Pore size distributions, calculated from the experimental isotherms based on a density functional theory model, confirm the hierarchical pore structure with the void diameters clustered around 10 and 38 Å (Figure S32). The excellent textural characteristics of these materials underscore their promise for applications such as catalysis, which rely on rapid mass transport through the support material to the active nanoparticle sites.

Inspired by this success, we sought to extend this methodology to the preparation of supported *tetrametallic* NPs. This was achieved by incorporating a combination of either (a) nickel(II)/copper(II)/iron(III) or (b) nickel(II)/copper(II)/terbium(III) into the tannic acid coordination polymer shell layer of the composite prior to thermolysis. This produced ZIF-8/Pt@NiCuFe-TA and ZIF-8/Pt@NiCuTb-TA. The presence of the expected set of metal components was confirmed by EDS (Figure S11).

The subsequent pyrolysis of these composites under reducing conditions resulted in the formation tetrametallic alloyed nanoparticles (either PtNiCuFe or PtNiCuTb), as revealed by electron microscopy, TEM, HRTEM, STEM mapping, SAED, and EDS. The TEM images and associated EDS line scans demonstrate that the MMNPs have uniform diameters that average ~7.3 nm and that the components are uniformly alloyed (Figure 5 and Figures S27, S28, and S30). HRTEM images of individual nanoparticles reveal lattice fringes with an interplanar distance of around 2.16 Å (PtNiCuFe) and 2.15 Å (PtNiCuTb) (Figure S27). As observed for the ternary nanoparticles, PXRD patterns are consistent with the quaternary nanoparticles retaining the fcc lattice of the PtNP seeds, but with shorter internuclear distances arising from the smaller average size of the constituent atoms (Figure 6a).

The BET surface areas of PtNiCuFe@NPCC and PtNiCuTb@NPCC, calculated from N_2 adsorption isotherms at 77 K, are 680 and 702 $m^2\ g^{-1}$, respectively (Figure 6b). Pore size distribution plots derived from these adsorption isotherms show hierarchical features similar to those seen in the trimetallic analogues (Figure S32).

ELECTROCATALYSIS

Improvements to the efficiency of the electrocatalytic splitting of water to produce hydrogen and oxygen will propel this technology toward implementation in sustainable energy devices.[31,32] The coupling of the HER and OER by so-called bifunctional catalysts is an attractive route to this goal.[33−35] Platinum nanomaterials often show excellent activities for HER but very low activity for OER.[15,27,36−38] Oxides of iridium and ruthenium are the most prominent electrocatalysts for the OER.[34,39−42] The major downsides of these benchmark catalysts are their price and lack of stability at high anodic potentials. This limits their practicality for large-scale applications. To overcome these drawbacks, while maintaining or improving catalytic activity, the investigation of multimetallic catalysts that combine noble metals with inexpensive non-noble metals—such as alloys or core–shell structures—has been shown to hold significant promise.[43−49] The exceptional electrocatalytic activity of multicomponent metal nanoparticle catalysts has been ascribed to synergistic effects among their components, which elevates their electrocatalytic activity above that of their single-component analogues.[50]

In this light, the synthetic methodology presented herein offers an avenue to the identification and optimization of catalysts. Rather than attempting to preselect catalysts in advance and/or synthesizing them in a serial fashion, diverse libraries of electrocatalysts can be produced in a combinatorial fashion. High-performance members of this library can subsequently be identified by high-throughput testing. As proof of concept, we conducted a series of experiments to assess the electrocatalytic performance and stability of the multicomponent nanoparticles described above. We anticipated that the carbon capsules would confer a significant benefit to the MMNP catalysts as their nitrogen doping, electrical conductivity, porosity, and hollow morphology should facilitate access of the substrates and electrons to the catalytic sites.[51−59] Furthermore, the capsules serve to localize and protect the nanoparticles, which would otherwise be prone to sintering or aggregating.

We tested the electrocatalytic HER performance of all materials using a rotating disk electrode at 1600 rpm in 1.0 M KOH. Commercial Pt on carbon (20% Pt) was measured as a comparison. The results are summarized in Table 2 and Figure 7. The foremost conclusion from these results is that the composition of the supported MMNPs dictates their catalytic ability, which underscores the utility of our synthetic methodology to generate diverse libraries. The supported PtNiCu and PtNiCuFe MMNP alloys are comparable in performance to Pt-only nanoparticles and to commercial Pt/C. This is significant because the Pt content of the PtNiCu and PtNiCuFe is low (Table 1). On the other hand, PtNi, PtNiFe, PtNiMn, and PtNiCuTb nanoparticles are poor catalysts, as indicated by their high overpotentials (>50 mV). Tafel plots indicate that while electron transfer rates measured for the new materials do not surpass that of commercial Pt/C, Pt@NPCC, PtNiCu@NPCC, and PtNiCuFe@NPCC are all kinetically competent (Figure 7). Furthermore, Pt@NPCC (233 mV), PtNiCu@NPCC (258 mV), and PtNiCuFe@NPCC (278 mV) demonstrate very low overpotentials at high current densities (100 $mA{\cdot}cm^{-2}$), which

DOI: 10.1021/acsnano.8b01022
ACS Nano 2018, 12, 4594–4604

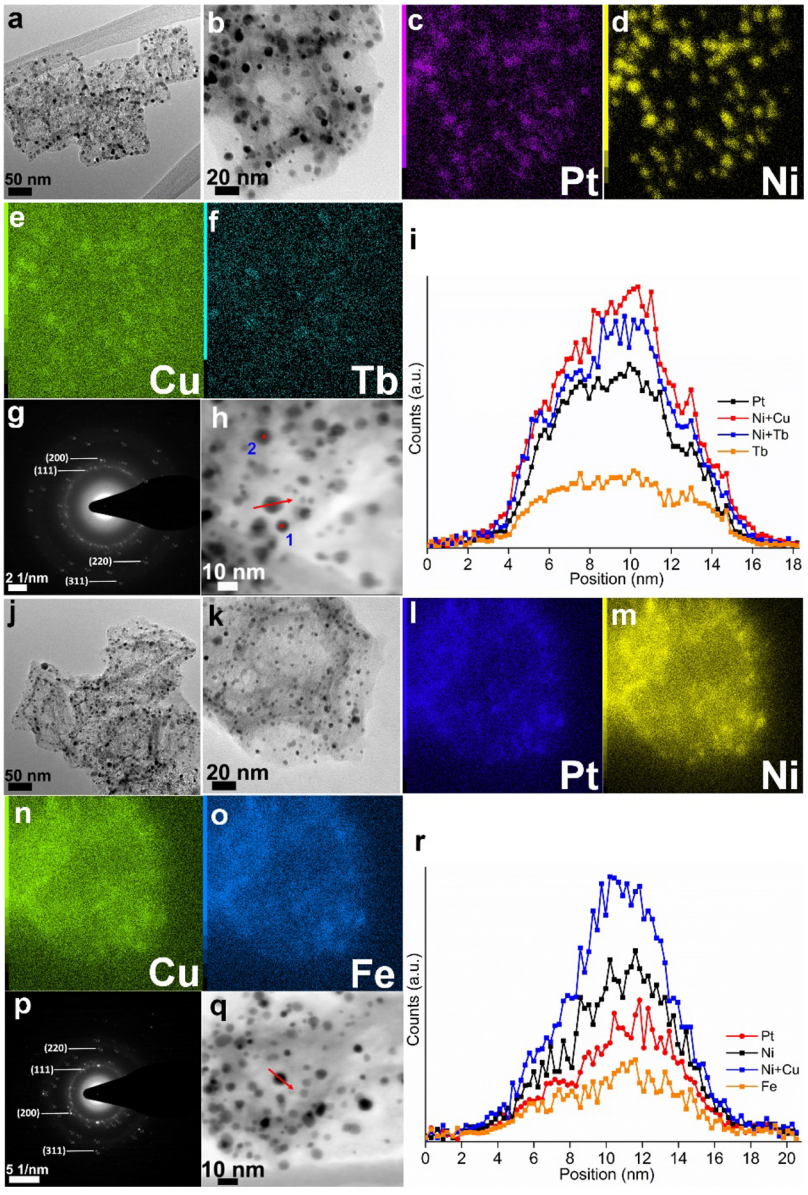

Figure 5. (a) TEM image of PtNiCuTb@NPCC. (b–f) STEM image and elemental mapping of PtNiCuTb@NPCC. (g) SAED pattern of PtNiCuTb@NPCC. (h,i) STEM image and linear distributions of Pt, Ni, Cu, and Tb along the arrow line on h. (j) TEM image of PtNiCuFe@NPCC. (k–o) STEM image and elemental mapping of PtNiCuFe@NPCC. (p) SAED pattern of PtNiCuFe@NPCC. (q,r) STEM image and linear distributions of Pt, Ni, Cu, and Fe along the arrow line on q.

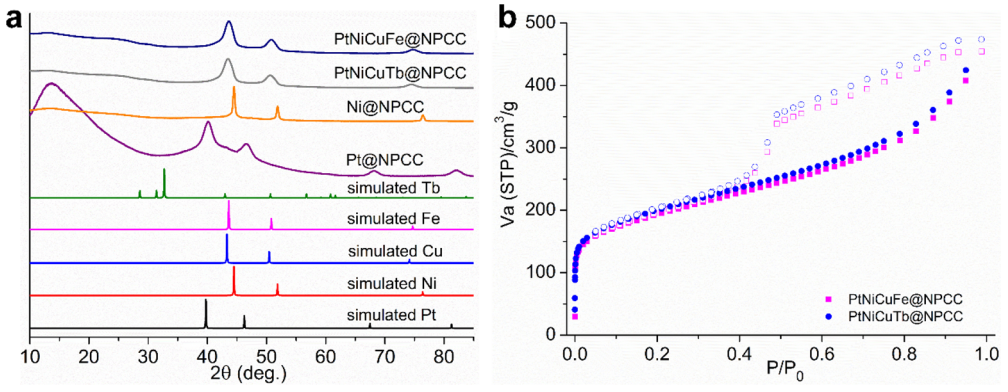

Figure 6. (a) PXRD patterns of the carbon-supported quaternary MMNPs. (b) Their N_2 adsorption (filled symbols) and desorption (open symbols) isotherms measured at 77 K.

DOI: 10.1021/acsnano.8b01022
ACS Nano 2018, 12, 4594–4604

Table 2. Summary of the HER and OER Activities of Selected Electrocatalysts Containing Monometallic and Multicomponent Metal Nanoparticles

Catalyst	HER η@10 mA[a]	HER Tafel slope[b]	OER η@10 mA[b]	OER Tafel slope[b]
Ni@NPCC	298	150	380	512
Pt@NPCC	30	63	410	149
PtNi@NPCC	118	72	380	94
PtNiFe@NPCC	83	68	330	79
PtNiCo@NPCC	69	64	370	99
PtNiTb@NPCC	126	97	380	144
PtNiCu@NPCC	38	65	350	131
PtNiMn@NPCC	90	87	380	152
PtNiCuFe@NPCC	40	63	300	148
PtNiCuTb@NPCC	82	96	340	147
commercial Pt/C	30	44	560	n/d
RuO_2	n/d	n/d	270	63

[a]HER η@10 mA cm^{-2} = the overpotential in mV for the hydrogen evolution reaction at a current density of 10 mA cm^{-2}. [b]In mV dec^{-1}. [d]OER η@ 10 mA cm^{-2} = the overpotential in mV for the oxygen evolution reaction at a current density of 10 mA cm^{-2}.

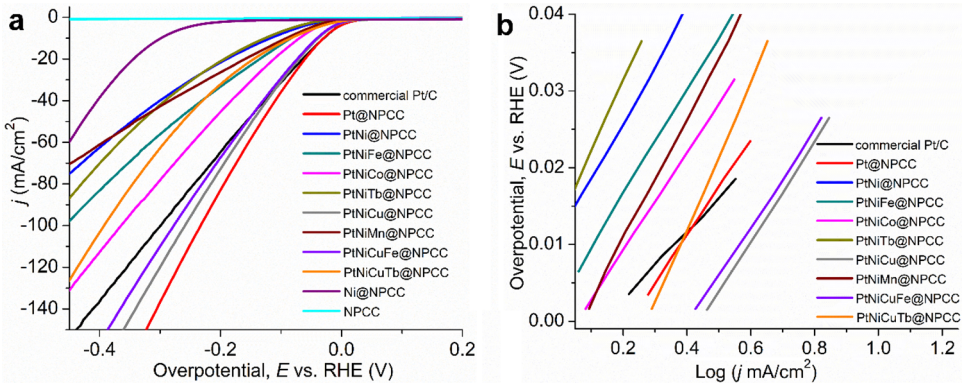

Figure 7. (a) HER polarization curves of selected catalysts in N_2-satuated 1.0 M KOH solution (scan rate = 5 mV s^{-1}; rotation rate = 1600 rpm). (b) Selected HER Tafel plots calculated from polarization curves. All overpotentials are given without *iR* correction.

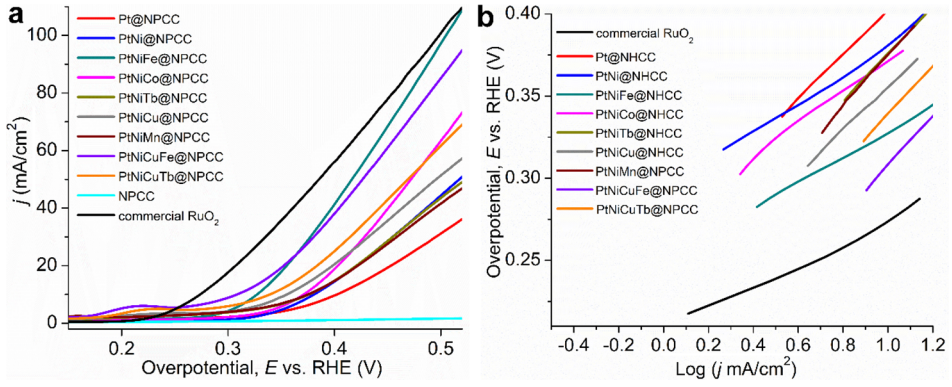

Figure 8. (a) OER polarization curves of selected catalysts in N_2-satuated 1.0 M KOH solution (scan rate = 5 mV s^{-1}; rotation rate = 1600 rpm). (b) Selected OER Tafel plots calculated from polarization curves. All overpotentials are given without *iR* correction.

meets the requirements for electrolysis under practical operating conditions. The activity of all these catalysts was retained after cycle testing 5000 times (Figure S48), confirming their durability. The catalytic ability of the high-performance materials identified by our approach is on par with the best HER catalysts previously reported in the literature (Table S2).

The OER performance of the newly synthesized materials was evaluated in 1.0 M KOH solution with the same electrode configuration as that used for the HER. Commercial RuO_2 was measured as a point of comparison. Linear sweep voltammetry experiments showed that the supported nanoparticles exhibit varying degrees of catalytic efficiency (Figure 8 and Table 2). From our library of new materials, the Pt, Ni, and PtNi nanoparticles were found to be poor OER catalysts. On the other hand, ternary and quaternary MMNPs are more effective, and we identified alloyed PtNiFe and PtNiCuFe MMNPs as outstanding catalysts. Their low platinum loadings have positive implications for the development of economical water splitting catalysts. The overpotential to deliver an anodic current density of 10 mA·cm^{-2} for PtNiCuFe@NPCC is only about 300 mV, which is the highest among the materials reported herein and comparable with the best catalysts reported for this reaction

DOI: 10.1021/acsnano.8b01022
ACS Nano 2018, 12, 4594−4604

(Table S3). The benchmark material RuO_2 exhibited a value of 270 mV (correlated to the potential of 1.53 V) under the same experimental conditions. Tafel plots indicate that PtNiFe@NPCC mediates a rapid rate of electron transfer (Figure 8 and Table 2).

Taken together, these results demonstrate that our methodology for synthesizing diverse libraries of supported MMNPs enables the rapid identification of efficient electrocatalysts. The most important aspect of our work is that *via* this strategy outstanding candidates will potentially emerge for any desired application. We are now focusing on extending our synthetic protocol to further diversify MMNP libraries, as well as exerting control over the ratio of the individual components in each example.

CONCLUSION

In summary, we have developed a powerful strategy for the synthesis of multicomponent metal nanoparticles embedded on porous carbon supports. Given the ready availability of the precursor materials, this methodology is potentially scalable to bulk quantities. Crucially, the assembly of the MMNP constituents in nanostructured precursor composites suppresses phase segregation at the nanoscale to produce alloyed particles. The ability to prepare libraries of nanoparticles in this way has parallels with combinatorial synthesis methods employed in organic synthesis. Extending this analogy, this strategy bypasses the demanding challenge of identifying high-performance materials for a target application *in advance* of their synthesis. Instead, an array of multicomponent nanoparticles can be produced by this synthetic method and subsequently screened against a performance assay to identify the elite nanoparticle compositions. In addition to driving forward the field of catalysis, this approach may find applications in plasmonics, medicine, and biological imaging.

EXPERIMENTAL SECTION

Full experimental details are included in the Supporting Information.

Synthesis of the ZIF-8/Pt@K-TA Composite. The ZIF-8/Pt@K-TA composite was prepared following our previously reported procedure.[25]

Synthesis of ZIF-8/Pt@Ni-TA, ZIF-8/Pt@NiM′-TA (M′ = Co, Cu, Mn, Fe, Tb), and Related Composites. For ZIF-8/Pt@Ni-TA synthesis, ZIF-8/Pt@K-TA was soaked in a methanolic solution (30 mL) of $Ni(NO_3)_2{\cdot}6H_2O$ (600 mg). After being stirred for 2 h, the ZIF-8@Ni-TA solid was collected by centrifugation, washed several times with methanol, and dried overnight under vacuum. Yield: 229 mg. For ZIF-8/Pt@NiCo-TA synthesis, a similar synthetic route was employed, only changing $Ni(NO_3)_2{\cdot}6H_2O$ to a $Ni(NO_3)_2{\cdot}6H_2O$ (600 mg)/$Co(NO_3)_2{\cdot}6H_2O$ (50 mg) mixture. Other materials were obtained *via* a similar synthetic route. ZIF-8/Pt@NiCu-TA: $Ni(NO_3)_2{\cdot}6H_2O$ (600 mg)/$Cu(NO_3)_2{\cdot}6H_2O$ (5 mg); ZIF-8/Pt@NiMn-TA: $Ni(NO_3)_2{\cdot}6H_2O$ (600 mg)/$Mn(NO_3)_2{\cdot}4H_2O$ (30 mg); ZIF-8/Pt@NiFe-TA: $Ni(NO_3)_2{\cdot}6H_2O$ (600 mg)/$Fe(NO_3)_2{\cdot}9H_2O$ (5 mg); ZIF-8/Pt@NiTb-TA: $Ni(NO_3)_2{\cdot}6H_2O$ (600 mg)/$Tb(NO_3)_2{\cdot}5H_2O$ (5 mg); ZIF-8/Pt@NiCuTb-TA: $Ni(NO_3)_2{\cdot}6H_2O$ (600 mg)/$Cu(NO_3)_2{\cdot}6H_2O$ (5 mg)/$Tb(NO_3)_2{\cdot}5H_2O$ (5 mg); and ZIF-8/Pt@NiCuFe-TA: $Ni(NO_3)_2{\cdot}6H_2O$ (600 mg)/$Cu(NO_3)_2{\cdot}6H_2O$ (5 mg)/$Fe(NO_3)_3{\cdot}9H_2O$ (5 mg).

Synthesis of PtNi@NPCC, PtNiFe@NPCC, PtNiCuFe@NPCC, and Related Composites. ZIF-8/Pt@Ni-TA was transferred into a ceramic crucible, placed in a furnace under a dry hydrogen (40%)/argon (60%) flow, and heated from room temperature to 900 °C over a period of 3 h. After the target temperature was reached, the sample was heated for a further 3 h at 900 °C and then cooled to room temperature to give PtNi@NPCC. PtNiCo@NPCC, PtNiCu@NPCC, PtNiMn@NPCC, PtNiFe@NPCC, PtNiTb@NPCC, PtNiCuTb@NPCC, and PtNiCuFe@NPCC were prepared using the same protocol.

Electrochemical Studies. The HER and OER tests were performed with a PINE electrochemical analyzer (AFMSRCE Electrode Rotator WaveDriver 20 bipotentiostat/galvanostat system, USA) in 1 M KOH electrolyte (N_2-rich) at room temperature. All electrochemical measurements were conducted in a standard three-electrode system with a platinum counter electrode and Ag/AgCl (3.5 M KCl) reference electrode. A glassy carbon rotating disk electrode (5.0 mm in diameter, 0.196 cm^2, PINE, USA) supported the as-synthesized materials to serve as the working electrode with a rotation speed of 1600 rpm. Five milligrams of sample was dispersed in 1.1 mL of ethanol and 100 μL of deionized water (containing 100 μL of 5.0 wt % Nafion) solution under ultrasonic agitation to form an electrocatalyst ink. The ink was dropped onto the surface of the precleaned rotating disk working electrode and dried at room temperature. The catalyst loading was determined to be 0.1 mg cm^{-2} (based on the total mass of catalyst). Commercial RuO_2 (loading ~0.8 mg) and commercial Pt/C (0.1 mg total mass, 20 wt % Pt) were prepared as catalysts using the same method for the purposes of comparison. Long-term stability tests for catalysts were conducted over 5000 cycles by measuring polarization curves with the linear sweep voltammetry technique.

ASSOCIATED CONTENT

Supporting Information

The Supporting Information is available free of charge on the ACS Publications website at DOI: 10.1021/acsnano.8b01022.

Additional experimental details and characterization data (PXRD, SEM, TEM, EDS, STEM, line scans, N_2 adsorption/desorption analysis, pore size distribution calculations, XPS, Raman and FTIR spectra, and electrochemical related curves and calculations) (PDF)

AUTHOR INFORMATION

Corresponding Authors

*E-mail: zhj@fjirsm.ac.cn.
*E-mail: paul.kruger@canterbury.ac.nz.
*E-mail: sqma@usf.edu.
*E-mail: s.telfer@massey.ac.nz.

ORCID

Thomas Nann: 0000-0002-2723-6553
Jian Zhang: 0000-0003-3373-9621
Paul E. Kruger: 0000-0003-4847-6780
Shengqian Ma: 0000-0002-1897-7069
Shane G. Telfer: 0000-0003-1596-6652

Notes

The authors declare no competing financial interest.

ACKNOWLEDGMENTS

We gratefully acknowledge the MacDiarmid Institute for financial support, particularly the postdoctoral fellowship to H.Y. We thank Jordan Taylor, Niki Minards, and Dr. Yusuf Emirov for expert assistance with the microscopy measurements, Haidee Dykstra and Associate Prof. Mark Waterland for kindly recording the Raman spectra, Dr. Kia Williams for technical assistance, and Dr. Tian-You Zhou for help with graphics.

REFERENCES

(1) Liu, H.; Nosheen, F.; Wang, X. Noble Metal Alloy Complex Nanostructures: Controllable Synthesis And Their Electrochemical Property. *Chem. Soc. Rev.* **2015**, *44*, 3056−3078.

DOI: 10.1021/acsnano.8b01022
ACS Nano 2018, 12, 4594−4604

(2) Gilroy, K. D.; Ruditskiy, A.; Peng, H.-C.; Qin, D.; Xia, Y. Bimetallic Nanocrystals: Syntheses, Properties, and Applications. *Chem. Rev.* **2016**, *116*, 10414−10472.
(3) Chen, A.; Ostrom, C. Palladium-Based Nanomaterials: Synthesis and Electrochemical Applications. *Chem. Rev.* **2015**, *115*, 11999−12044.
(4) Sankar, M.; Dimitratos, N.; Miedziak, P. J.; Wells, P. P.; Kiely, C. J.; Hutchings, G. J. Designing Bimetallic Catalysts For a Green and Sustainable Future. *Chem. Soc. Rev.* **2012**, *41*, 8099−8139.
(5) Weiner, R. G.; Kunz, M. R.; Skrabalak, S. E. Seeding a New Kind of Garden: Synthesis of Architecturally Defined Multimetallic Nanostructures by Seed-Mediated Co-Reduction. *Acc. Chem. Res.* **2015**, *48*, 2688−2695.
(6) Ferrando, R.; Jellinek, J.; Johnston, R. L. Nanoalloys: From Theory to Applications of Alloy Clusters and Nanoparticles. *Chem. Rev.* **2008**, *108*, 845−910.
(7) Chen, P.-C.; Liu, G.; Zhou, Y.; Brown, K. A.; Chernyak, N.; Hedrick, J. L.; He, S.; Xie, Z.; Lin, Q.-Y.; Dravid, V. P.; O'Neill-Slawecki, S. A.; Mirkin, C. A. Tip-Directed Synthesis of Multimetallic Nanoparticles. *J. Am. Chem. Soc.* **2015**, *137*, 9167−9173.
(8) Wu, Y.; Wang, D.; Chen, X.; Zhou, G.; Yu, R.; Li, Y. Defect-Dominated Shape Recovery of Nanocrystals: A New Strategy for Trimetallic Catalysts. *J. Am. Chem. Soc.* **2013**, *135*, 12220−12223.
(9) Kang, S. W.; Lee, Y. W.; Park, Y.; Choi, B.-S.; Hong, J. W.; Park, K.-H.; Han, S. W. One-Pot Synthesis of Trimetallic Au@PdPt Core−Shell Nanoparticles with High Catalytic Performance. *ACS Nano* **2013**, *7*, 7945−7955.
(10) Huang, X.; Zhao, Z.; Cao, L.; Chen, Y.; Zhu, E.; Lin, Z.; Li, M.; Yan, A.; Zettl, A.; Wang, Y. M.; Duan, X.; Mueller, T.; Huang, Y. High-Performance Transition Metal−Doped Pt_3Ni Octahedra For Oxygen Reduction Reaction. *Science* **2015**, *348*, 1230−1234.
(11) Kuroki, H.; Tamaki, T.; Matsumoto, M.; Arao, M.; Kubobuchi, K.; Imai, H.; Yamaguchi, T. Platinum−Iron−Nickel Trimetallic Catalyst with Superlattice Structure for Enhanced Oxygen Reduction Activity and Durability. *Ind. Eng. Chem. Res.* **2016**, *55*, 11458−11466.
(12) Zhu, H.; Zhang, S.; Guo, S.; Su, D.; Sun, S. Synthetic Control of FePtM Nanorods (M = Cu, Ni) To Enhance the Oxygen Reduction Reaction. *J. Am. Chem. Soc.* **2013**, *135*, 7130−7133.
(13) Li, H.; Ren, C.; Xu, S.; Wang, L.; Yue, Q.; Li, R.; Zhang, Y.; Xue, Q.; Liu, J. Te-Template Approach To Fabricating Ternary Tecupt Alloy Nanowires With Enhanced Catalytic Performance Towards Oxygen Reduction Reaction And Methanol Oxidation Reaction. *J. Mater. Chem. A* **2015**, *3*, 5850−5858.
(14) Ma, S.-Y.; Li, H.-H.; Hu, B.-C.; Cheng, X.; Fu, Q.-Q.; Yu, S.-H. Synthesis of Low Pt-Based Quaternary PtPdRuTe Nanotubes with Optimized Incorporation of Pd for Enhanced Electrocatalytic Activity. *J. Am. Chem. Soc.* **2017**, *139*, 5890−5895.
(15) Cai, B.; Dianat, A.; Hübner, R.; Liu, W.; Wen, D.; Benad, A.; Sonntag, L.; Gemming, T.; Cuniberti, G.; Eychmüller, A. Multimetallic Hierarchical Aerogels: Shape Engineering of the Building Blocks for Efficient Electrocatalysis. *Adv. Mater.* **2017**, *29*, 1605254.
(16) Chen, C.; Kang, Y.; Huo, Z.; Zhu, Z.; Huang, W.; Xin, H. L.; Snyder, J. D.; Li, D.; Herron, J. A.; Mavrikakis, M.; Chi, M.; More, K. L.; Li, Y.; Markovic, N. M.; Somorjai, G. A.; Yang, P.; Stamenkovic, V. R. Highly Crystalline Multimetallic Nanoframes with Three-Dimensional Electrocatalytic Surfaces. *Science* **2014**, *343*, 1339−1343.
(17) Ud Din, M. A.; Saleem, F.; Ni, B.; Yong, Y.; Wang, X. Porous Tetrametallic PtCuBiMn Nanosheets with a High Catalytic Activity and Methanol Tolerance Limit for Oxygen Reduction Reactions. *Adv. Mater.* **2017**, *29*, 1604994.
(18) Zhou, Z.; Hu, K.; Ma, R.; Yan, Y.; Ni, B.; Zhang, Y.; Wen, L.; Zhang, Q.; Cheng, Y. Dendritic Platinum−Copper Alloy Nanoparticles as Theranostic Agents for Multimodal Imaging and Combined Chemophotothermal Therapy. *Adv. Funct. Mater.* **2016**, *26*, 5971−5978.
(19) Ye, X.; Shi, H.; He, X.; Yu, Y.; He, D.; Tang, J.; Lei, Y.; Wang, K. Cu-Au Alloy Nanostructures Coated With Aptamers: A Simple, Stable And Highly Effective Platform For In *Vivo* Cancer Theranostics. *Nanoscale* **2016**, *8*, 2260−2267.
(20) Song, X.-R.; Yu, S.-X.; Jin, G.-X.; Wang, X.; Chen, J.; Li, J.; Liu, G.; Yang, H.-H. Plant Polyphenol-Assisted Green Synthesis of Hollow CoPt Alloy Nanoparticles for Dual-Modality Imaging Guided Photothermal Therapy. *Small* **2016**, *12*, 1506−1513.
(21) Chen, S.; Wang, L.; Duce, S. L.; Brown, S.; Lee, S.; Melzer, A.; Cuschieri, S. A.; André, P. Engineered Biocompatible Nanoparticles for in *Vivo* Imaging Applications. *J. Am. Chem. Soc.* **2010**, *132*, 15022−15029.
(22) Lu, Y.; Shi, C.; Hu, M.-J.; Xu, Y.-J.; Yu, L.; Wen, L.-P.; Zhao, Y.; Xu, W.-P.; Yu, S.-H. Magnetic Alloy Nanorings Loaded with Gold Nanoparticles: Synthesis and Applications as Multimodal Imaging Contrast Agents. *Adv. Funct. Mater.* **2010**, *20*, 3701−3706.
(23) Amendola, V.; Scaramuzza, S.; Litti, L.; Meneghetti, M.; Zuccolotto, G.; Rosato, A.; Nicolato, E.; Marzola, P.; Fracasso, G.; Anselmi, C.; Pinto, M.; Colombatti, M. Magneto-Plasmonic Au-Fe Alloy Nanoparticles Designed for Multimodal SERS-MRI-CT Imaging. *Small* **2014**, *10*, 2476−2486.
(24) Chen, P.-C.; Liu, X.; Hedrick, J. L.; Xie, Z.; Wang, S.; Lin, Q.-Y.; Hersam, M. C.; Dravid, V. P.; Mirkin, C. A. Polyelemental Nanoparticle Libraries. *Science* **2016**, *352*, 1565−1569.
(25) Yang, H.; Bradley, S. J.; Chan, A.; Waterhouse, G. I. N.; Nann, T.; Kruger, P. E.; Telfer, S. G. Catalytically Active Bimetallic Nanoparticles Supported on Porous Carbon Capsules Derived From Metal−Organic Framework Composites. *J. Am. Chem. Soc.* **2016**, *138*, 11872−11881.
(26) Nanda, K. K.; Sahu, S. N.; Behera, S. N. Liquid-Drop Model For The Size-Dependent Melting Of Low-Dimensional Systems. *Phys. Rev. A: At., Mol., Opt. Phys.* **2002**, *66*, 013208.
(27) Yin, H.; Zhao, S.; Zhao, K.; Muqsit, A.; Tang, H.; Chang, L.; Zhao, H.; Gao, Y.; Tang, Z. Ultrathin Platinum Nanowires Grown On Single-Layered Nickel Hydroxide With High Hydrogen Evolution Activity. *Nat. Commun.* **2015**, *6*, 6430.
(28) Wanjala, B. N.; Fang, B.; Luo, J.; Chen, Y.; Yin, J.; Engelhard, M. H.; Loukrakpam, R.; Zhong, C.-J. Correlation between Atomic Coordination Structure and Enhanced Electrocatalytic Activity for Trimetallic Alloy Catalysts. *J. Am. Chem. Soc.* **2011**, *133*, 12714−12727.
(29) Yang, D. Q.; Sacher, E. Characterization and Oxidation of Fe Nanoparticles Deposited onto Highly Oriented Pyrolytic Graphite, Using X-ray Photoelectron Spectroscopy. *J. Phys. Chem. C* **2009**, *113*, 6418−6425.
(30) Easterday, R.; Sanchez-Felix, O.; Stein, B. D.; Morgan, D. G.; Pink, M.; Losovyj, Y.; Bronstein, L. M. Structural Study of Pt−Fe Nanoparticles: New Insights into Pt Bimetallic Nanoparticle Formation with Oxidized Fe Species. *J. Phys. Chem. C* **2014**, *118*, 24769−24775.
(31) Dresselhaus, M. S.; Thomas, I. L. Alternative Energy Technologies. *Nature* **2001**, *414*, 332−337.
(32) Gu, S.; Xu, B.; Yan, Y. Electrochemical Energy Engineering: A New Frontier of Chemical Engineering Innovation. *Annu. Rev. Chem. Biomol. Eng.* **2014**, *5*, 429−454.
(33) McCrory, C. C. L.; Jung, S.; Ferrer, I. M.; Chatman, S. M.; Peters, J. C.; Jaramillo, T. F. Benchmarking Hydrogen Evolving Reaction and Oxygen Evolving Reaction Electrocatalysts for Solar Water Splitting Devices. *J. Am. Chem. Soc.* **2015**, *137*, 4347−4357.
(34) Suen, N.-T.; Hung, S.-F.; Quan, Q.; Zhang, N.; Xu, Y.-J.; Chen, H. M. Electrocatalysis For the Oxygen Evolution Reaction: Recent Development and Future Perspectives. *Chem. Soc. Rev.* **2017**, *46*, 337−365.
(35) Morales-Guio, C. G.; Stern, L.-A.; Hu, X. Nanostructured Hydrotreating Catalysts For Electrochemical Hydrogen Evolution. *Chem. Soc. Rev.* **2014**, *43*, 6555−6569.
(36) Barber, J. H.; Conway, B. E. Structural Specificity Of The Kinetics Of The Hydrogen Evolution Reaction On the Low-Index Surfaces Of Pt Single-Crystal Electrodes In 0.5 M dm^{-3} NaOH. *J. Electroanal. Chem.* **1999**, *461*, 80−89.
(37) Durst, J.; Siebel, A.; Simon, C.; Hasche, F.; Herranz, J.; Gasteiger, H. A. New Insights Into the Electrochemical Hydrogen

DOI: 10.1021/acsnano.8b01022
ACS Nano 2018, 12, 4594−4604

Oxidation and Evolution Reaction Mechanism. *Energy Environ. Sci.* **2014**, *7*, 2255−2260.
(38) Sheng, W.; Myint, M.; Chen, J. G.; Yan, Y. Correlating The Hydrogen Evolution Reaction Activity In Alkaline Electrolytes With The Hydrogen Binding Energy On Monometallic Surfaces. *Energy Environ. Sci.* **2013**, *6*, 1509−1512.
(39) Mattos-Costa, F. I.; de Lima-Neto, P.; Machado, S. A. S.; Avaca, L. A. Characterisation Of Surfaces Modified by Sol-Gel Derived $Ruxir_{1-x}o_2$ Coatings for Oxygen Evolution in Acid Medium. *Electrochim. Acta* **1998**, *44*, 1515−1523.
(40) Lee, Y.; Suntivich, J.; May, K. J.; Perry, E. E.; Shao-Horn, Y. Synthesis and Activities of Rutile IrO_2 and RuO_2 Nanoparticles for Oxygen Evolution in Acid and Alkaline Solutions. *J. Phys. Chem. Lett.* **2012**, *3*, 399−404.
(41) Audichon, T.; Napporn, T. W.; Canaff, C.; Morais, C.; Comminges, C.; Kokoh, K. B. IrO_2 Coated on RuO_2 as Efficient and Stable Electroactive Nanocatalysts for Electrochemical Water Splitting. *J. Phys. Chem. C* **2016**, *120*, 2562−2573.
(42) Vuković, M. Oxygen Evolution Reaction On Thermally Treated Iridium Oxide Films. *J. Appl. Electrochem.* **1987**, *17*, 737−745.
(43) Oh, A.; Sa, Y. J.; Hwang, H.; Baik, H.; Kim, J.; Kim, B.; Joo, S. H.; Lee, K. Rational Design Of Pt-Ni-Co Ternary Alloy Nanoframe Crystals As Highly Efficient Catalysts Toward The Alkaline Hydrogen Evolution Reaction. *Nanoscale* **2016**, *8*, 16379−16386.
(44) Du, N.; Wang, C.; Wang, X.; Lin, Y.; Jiang, J.; Xiong, Y. Trimetallic TriStar Nanostructures: Tuning Electronic and Surface Structures for Enhanced Electrocatalytic Hydrogen Evolution. *Adv. Mater.* **2016**, *28*, 2077−2084.
(45) Wang, S.; Yang, G.; Yang, S. Pt-Frame@Ni quasi Core−Shell Concave Octahedral $PtNi_3$ Bimetallic Nanocrystals for Electrocatalytic Methanol Oxidation and Hydrogen Evolution. *J. Phys. Chem. C* **2015**, *119*, 27938−27945.
(46) Reier, T.; Pawolek, Z.; Cherevko, S.; Bruns, M.; Jones, T.; Teschner, D.; Selve, S.; Bergmann, A.; Nong, H. N.; Schlögl, R.; Mayrhofer, K. J. J.; Strasser, P. Molecular Insight in Structure and Activity of Highly Efficient, Low-Ir Ir−Ni Oxide Catalysts for Electrochemical Water Splitting (OER). *J. Am. Chem. Soc.* **2015**, *137*, 13031−13040.
(47) Papaderakis, A.; Pliatsikas, N.; Prochaska, C.; Vourlias, G.; Patsalas, P.; Tsiplakides, D.; Balomenou, S.; Sotiropoulos, S. Oxygen Evolution at IrO_2 Shell−Ir−Ni Core Electrodes Prepared by Galvanic Replacement. *J. Phys. Chem. C* **2016**, *120*, 19995−20005.
(48) Ma, L.; Luo, X.; Kropf, A. J.; Wen, J.; Wang, X.; Lee, S.; Myers, D. J.; Miller, D.; Wu, T.; Lu, J.; Amine, K. Insight into the Catalytic Mechanism of Bimetallic Platinum−Copper Core−Shell Nanostructures for Nonaqueous Oxygen Evolution Reactions. *Nano Lett.* **2016**, *16*, 781−785.
(49) Nong, H. N.; Gan, L.; Willinger, E.; Teschner, D.; Strasser, P. IrO_x Core-Shell Nanocatalysts For Cost- And Energy-Efficient Electrochemical Water Splitting. *Chem. Sci.* **2014**, *5*, 2955−2963.
(50) Aijaz, A.; Masa, J.; Rösler, C.; Xia, W.; Weide, P.; Botz, A. J. R.; Fischer, R. A.; Schuhmann, W.; Muhler, M. $Co@Co_3O_4$ Encapsulated in Carbon Nanotube-Grafted Nitrogen-Doped Carbon Polyhedra as an Advanced Bifunctional Oxygen Electrode. *Angew. Chem., Int. Ed.* **2016**, *55*, 4087−4091.
(51) Ikeda, S.; Ishino, S.; Harada, T.; Okamoto, N.; Sakata, T.; Mori, H.; Kuwabata, S.; Torimoto, T.; Matsumura, M. Ligand-Free Platinum Nanoparticles Encapsulated in a Hollow Porous Carbon Shell as a Highly Active Heterogeneous Hydrogenation Catalyst. *Angew. Chem., Int. Ed.* **2006**, *45*, 7063−7066.
(52) Wang, G. H.; Hilgert, J.; Richter, F. H.; Wang, F.; Bongard, H. J.; Spliethoff, B.; Weidenthaler, C.; Schuth, F. Platinum-Cobalt Bimetallic Nanoparticles in Hollow Carbon Nanospheres for Hydrogenolysis of 5-Hydroxymethylfurfural. *Nat. Mater.* **2014**, *13*, 293−300.
(53) Liu, R.; Mahurin, S. M.; Li, C.; Unocic, R. R.; Idrobo, J. C.; Gao, H.; Pennycook, S. J.; Dai, S. Dopamine As A Carbon Source: The Controlled Synthesis of Hollow Carbon Spheres and Yolk-Structured Carbon Nanocomposites. *Angew. Chem., Int. Ed.* **2011**, *50*, 6799−802.
(54) Galeano, C.; Baldizzone, C.; Bongard, H.; Spliethoff, B.; Weidenthaler, C.; Meier, J. C.; Mayrhofer, K. J. J.; Schüth, F. Carbon-Based Yolk−Shell Materials for Fuel Cell Applications. *Adv. Funct. Mater.* **2014**, *24*, 220−232.
(55) Liu, J.; Wu, C.; Xiao, D.; Kopold, P.; Gu, L.; van Aken, P. A.; Maier, J.; Yu, Y. MOF-Derived Hollow Co_9S_8 Nanoparticles Embedded in Graphitic Carbon Nanocages with Superior Li-Ion Storage. *Small* **2016**, *12*, 2354−2364.
(56) Galeano, C.; Meier, J. C.; Soorholtz, M.; Bongard, H.; Baldizzone, C.; Mayrhofer, K. J. J.; Schuth, F. Nitrogen-Doped Hollow Carbon Spheres as a Support for Platinum-Based Electrocatalysts. *ACS Catal.* **2014**, *4*, 3856−3868.
(57) Xu, X.; Nosheen, F.; Wang, X. Ni-Decorated Molybdenum Carbide Hollow Structure Derived from Carbon-Coated Metal−Organic Framework for Electrocatalytic Hydrogen Evolution Reaction. *Chem. Mater.* **2016**, *28*, 6313−6320.
(58) Ferrero, G. A.; Preuss, K.; Marinovic, A.; Jorge, A. B.; Mansor, N.; Brett, D. J. L.; Fuertes, A. B.; Sevilla, M.; Titirici, M.-M. Fe−N-Doped Carbon Capsules with Outstanding Electrochemical Performance and Stability for the Oxygen Reduction Reaction in Both Acid and Alkaline Conditions. *ACS Nano* **2016**, *10*, 5922−5932.
(59) Wang, H.; Wang, W.; Xu, Y. Y.; Dong, S.; Xiao, J.; Wang, F.; Liu, H.; Xia, B. Y. Hollow Nitrogen-Doped Carbon Spheres with Fe_3O_4 Nanoparticles Encapsulated as a Highly Active Oxygen-Reduction Catalyst. *ACS Appl. Mater. Interfaces* **2017**, *9*, 10610−10617.

DOI: 10.1021/acsnano.8b01022
ACS Nano 2018, 12, 4594−4604